metals

MDPI

Article

Investigation of the Machined Surface Integrity of WC-High-Entropy Alloy Cemented Carbide

Yandong Yin [1,2], Jin Du [1,2,*], Yujing Sun [1,2], Yan Xia [1,2], Peirong Zhang [1,2] and Guosheng Su [1,2]

[1] School of Mechanical Engineering, Qilu University of Technology (Shandong Academy of Sciences), Jinan 250353, China; 10431210050@stu.qlu.edu.cn (Y.Y.); sunyujing@qlu.edu.cn (Y.S.); yxia@qlu.edu.cn (Y.X.); sduzhangpeirong@gmail.com (P.Z.); sgs@qlu.edu.cn (G.S.)
[2] Shandong Institute of Mechanical Design and Research, Jinan 250031, China
* Correspondence: dj84105@126.com

Abstract: A fine-grained WC-15wt%$Al_{0.5}$CoCrFeNi cemented carbide was prepared through a vacuum and gas pressure sintering. For achieving high surface integrity, diamond wheel grinding serves as the primary molding process for the machining of WC cemented carbide. To reveal the influence of grinding on the surface integrity of fine-grained WC-HEA cemented carbide, studies were conducted on grinding force, surface microstructure, surface roughness, residual stress, microhardness, and bending strength. The morphological analysis of the ground surface indicated a transition in the material removal mechanism of WC-HEA cemented carbide from ductile removal to brittle removal, with brittle removal becoming predominant as the depth of grinding increases. With the increasing depth of grinding, the grinding force increases, and the grinding force increases while the surface roughness decreases. Correspondingly, there is an improvement in both hardness and bending strength. Additionally, grinding induces high residual compressive stress on the surface, with a maximum compressive stress of 1795 MPa. The bending strength of the material is found to be dependent on the residual stress.

Keywords: WC-HEA cemented carbide; grinding; surface integrity

check for updates

Citation: Yin, Y.; Du, J.; Sun, Y.; Xia, Y.; Zhang, P.; Su, G. Investigation of the Machined Surface Integrity of WC-High-Entropy Alloy Cemented Carbide. *Metals* **2024**, *14*, 419. https://doi.org/10.3390/met14040419

Academic Editor: Yadir Torres Hernández

Received: 5 March 2024
Revised: 28 March 2024
Accepted: 1 April 2024
Published: 3 April 2024

Copyright: © 2024 by the authors. Licensee MDPI, Basel, Switzerland. This article is an open access article distributed under the terms and conditions of the Creative Commons Attribution (CC BY) license (https://creativecommons.org/licenses/by/4.0/).

1. Introduction

WC-based cemented carbides are known for their exceptional performance and find wide applications in cutting tools, molds, and wear-resistant components [1]. Co is the most commonly used binder phase in WC-based cemented carbides. However, WC-Co alloys have poor corrosion resistance, inferior high-temperature performance, and are harmful to human health [2,3]. In contrast, high-entropy alloys (HEAs) possess high hardness, excellent corrosion resistance, and good resistance relative to high-temperature oxidation [4–7]. By replacing Co as the binder phase in WC-HEA alloys, the performance has also been improved significantly. Chen et al. prepared WC-HEA alloys using mechanical alloying; the hardness of the bodies made of such alloy at high temperatures measured at 900 °C was 200 HV higher than that of the bodies made of WC-Co alloys [8]. Similarly, WC-Co and WC-HEA alloys were fabricated through hot-pressure sintering, and the test results confirm that the WC-HEA alloy exhibited superior mechanical properties and corrosion resistance [9].

WC-HEA alloys are extremely difficult materials to machine, and they are characterized by "high hardness and high brittleness". There are some problems in the mechanical machining process, such as susceptibility to damage, low processing efficiency, and poor surface integrity. To address these challenges and meet the requirements for geometric precision of workpiece surfaces, diamond wheel grinding has emerged as the primary machining method [10,11].

The surface of the diamond wheel is covered with irregularly shaped abrasive grains, which can be regarded as multiple blades collectively cutting the material surface, constituting a complex machining process. The removal mechanisms of hard and brittle materials, represented by metal ceramics, generally involve two modes: brittle removal and ductile removal [12,13]. Klocke et al. [14] conducted a single grain cutting test on the WC-Co alloy, where scratches indicated a transition from ductile to brittle removal mechanisms, predominantly characterized by brittle removal mechanisms. Wirtz et al. [15] conducted a microscopic analysis of scratches, elucidating the removal mechanisms of WC-Co alloy materials: As the abrasive grains begin to penetrate the surface of the material, cracks appear within the WC grains; under the influence of thermal and mechanical coupling, these cracks propagate, leading to surface fracture; with increasing grinding depth, noticeable bulging is observed on both sides of the scratch; subsequently, sporadic flaking occurs on the material surface, followed by continuous and extensive fracturing, marking a transition from ductile to brittle removal mechanisms. Muller et al. [16] employed a combined methodology that integrates single abrasive grain scratching experiments with material removal models and elucidated the dependence of material removal behavior on the cutting depth of abrasive grains and the transition from predominantly ductile to brittle behavior characterized by cracking and fracturing in WC-Co alloys' ground surfaces. Additionally, the machining scale is an important condition for the ductile machining of brittle materials [17].

Grinding is a process where numerous abrasive grains act simultaneously. Clearly, the single grain cutting test has certain limitations in revealing the material removal process. Grinding significantly alters the integrity of the surface and subsurface, particularly in terms of deformation, phase transformation, damage, residual stress, and bending strength in the surface and subsurface. Hegeman [11] discovered a deformed layer of about 1.5 μm on the surface of the alloy after grinding, composed of the binder phase Co and partially fractured WC grains. The stress in this layer is mainly residual compressive stress, and the plastic deformation of WC grains occurs beneath the transformation layer. Research by Yang et al. [18] showed that the binder phase Co in the alloy, after grinding, transformed from fcc to hcp, and the depth of the phase transformation coincided with the distribution of residual stress, indicating that the residual stress is the result of the combined effects of phase transformation, plastic deformation, and grain refinement. Yang et al. [19] found subsurface damage of about 400 nm below the ground surface, mainly characterized by fractured WC grains, exhibiting intergranular or transgranular fracture. Furthermore, high residual compressive stress exists on the ground surface, with stress decreasing as the depth from the ground surface increases. Simultaneously, the mechanical properties (hardness and bending strength) of the ground surface are correspondingly improved. Yin et al. [20] conducted grinding experiments on alloys with different WC grain sizes and found that residual stress induced by grinding increases with decreasing WC grain size, and no grinding-induced cracks were observed on the surface. Zhang et al. [21] ground WC-Co and WC without a binder phase and found that the surface roughness of WC-Co was lower than that of WC without a binder phase. This is partly because Co is extruded, reducing the binder phase, causing WC to detach, and leaving pits; on the other hand, the removal rates of Co and WC differ, resulting in different heights between WC and the binder phase.

As mentioned above, the changes in the material removal mechanisms and surface integrity of traditional WC-Co alloys during machining are well studied. However, there is scarce research on the machinability aspect of WC-HEA alloys, where HEA acts as the binder phase. This investigation aims to reveal the material removal mechanisms during the grinding of WC-HEA alloys, illustrating the effect of the grinding process on the machined surface integrity. This study analyzes and investigates the surface and subsurface morphology, elemental composition, surface roughness, residual stress, bending strength, and hardness of WC-HEA cemented carbide after grinding.

2. Materials and Experimental Procedures

2.1. Experimental Material

High-purity (99.5%) $Al_{0.5}CoCrFeNi$ powder, with an average particle size of less than 25 μm, was prepared using vacuum atomization technology. The HEA powder (15 wt.%) was blended with WC powder (85 wt.%) in a ball milling jar containing balls and a jar made of cemented carbide material, using a ball–powder ratio of 10:1. Mechanical alloying was conducted in a ball mill at a rotation speed of 80 r/min for 64 h. After wet milling, the slurry obtained was filtered through a 350-mesh sieve and dried for 90 min in a vacuum drying oven at 110 °C to obtain WC-HEA powder.

The cooled WC-HEA powder was mixed with a paraffin and gasoline mixture in a liquid state, and then sieved through a 100-mesh sieve after drying for 20 min. Subsequently, under a pressure of 200 MPa, the WC-HEA powder was pressed into billets with dimensions of 20 mm × 8 mm × 6 mm with a PM hydraulic press. Finally, the WC-HEA samples were prepared using a composite sintering method. Following vacuum sintering and cooling to room temperature, pressure sintering reinforcement was applied, as shown in Figure 1.

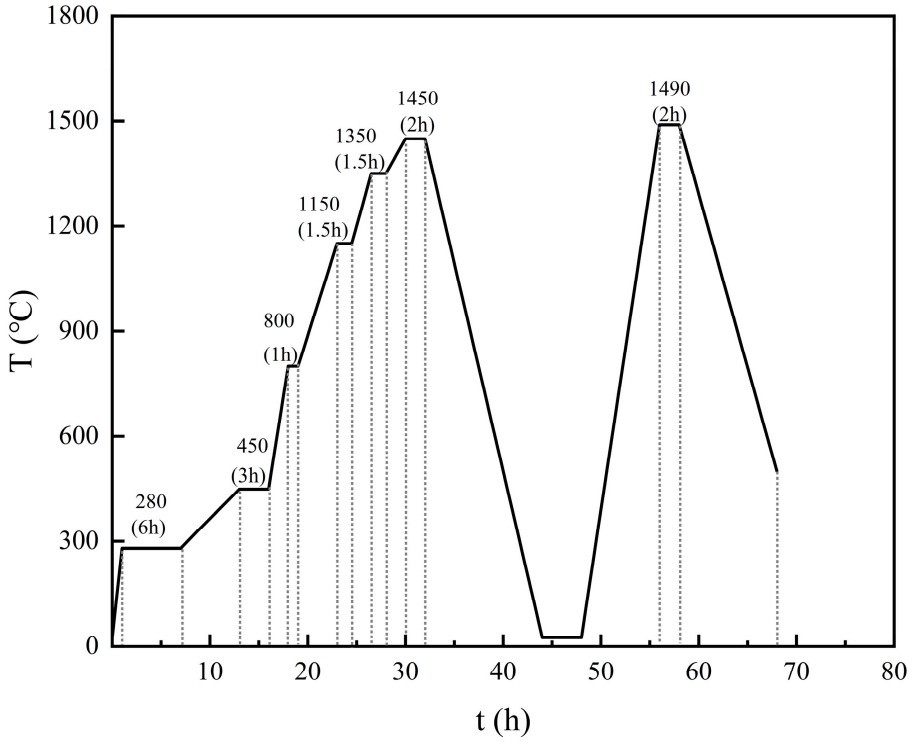


Figure 1. Sintering curve of WC-HEA cemented carbide.

The backscattered electron (BSE) imaging technique of the scanning electron microscope (FEI QUANTA FEG250 (Quanta, Waltham, MA, USA)) was utilized to observe the microstructure of the specimen after sintering. Figure 2a shows the microstructure of the WC-HEA, where the grey regions represent WC grains, and the black regions represent the HEA binder phase. The WC average grain size of the WC-HEA alloy was measured as 0.97 μm by ImageJ software ((Fii ls Just) lmage 214.0/154f, Java 1.8.0 322 [64-bit]), indicating that it is a fine-grained alloy, as shown in Figure 2b.

The physical and mechanical properties of WC-HEA alloy were evaluated [22], including relative density, hardness (HV), fracture toughness (K_{IC}), and bending strength (TRS), and they are presented in Table 1. To assess the material's flexural strength, strength tests were conducted using the universal testing machine AGS-X5KN (Shimadzu, Kyoto, Japan). The Vickers hardness of the samples was measured using a microhardness tester (HVS-50 (Huayin, Laizhou, SD, China)). The depth-of-focus microscope (VHX-5000 (Keyence, Osaka,

Japan)) was utilized to measure the diagonal length of the indentation and crack length. The fracture toughness was calculated using the following formula [23]:

$$K_I C = 0.15 \sqrt{\frac{HV_{30}}{\sum_{i=1}^{4} L_i}} \quad (1)$$

where K_{IC} represents the fracture toughness (MPa·m$^{1/2}$), HV_{30} denotes the Vickers hardness (MPa), and L_i stands for the crack length of the indentation (mm). Five samples were measured, and the average value was obtained.

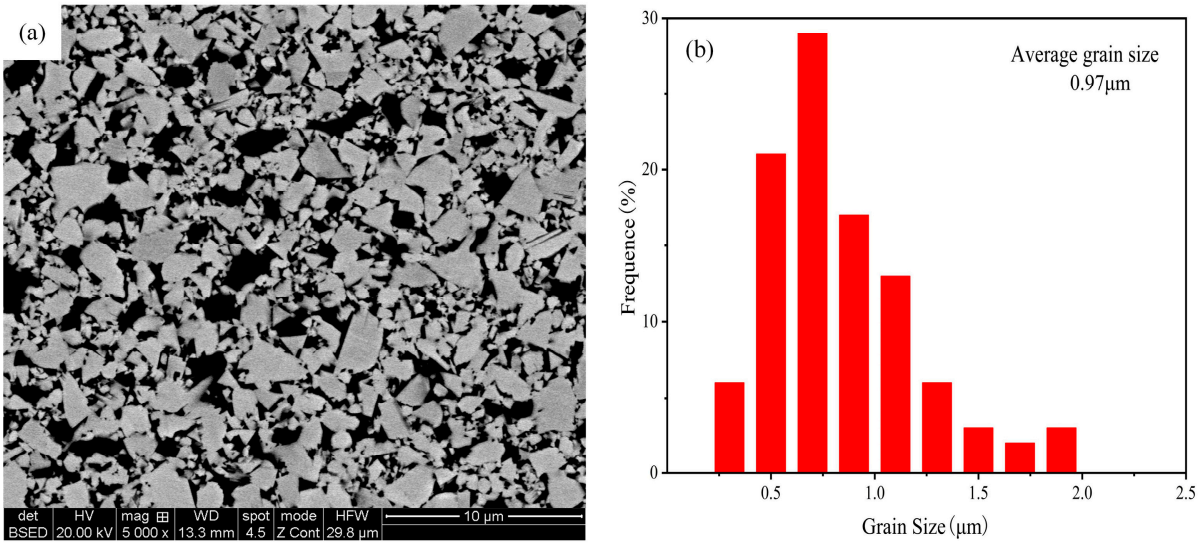


Figure 2. (**a**) Microstructure of the WC-HEA and (**b**) the distribution of average grain sizes.

Table 1. The physical and mechanical property parameters of the material.

Material	Relative Density (%)	Hardness (HV)	K_{IC} (MPa·m$^{1/2}$)	TRS(MPa)
WC-HEA	92.3	1537.8	8.7	890

2.2. Grinding Procedure

The grinding experiment was carried out using the surface grinding machine M7163 × 12-GM. The abrasive wheel utilized a resin binder, with diamond grains sized at 240 mesh. Operating with a diameter of 400 mm, the grinding wheel rotated at a speed of 1440 r/min. Figure 3 shows the grinding system, consisting of a diamond grinding wheel, workpiece, fixture, and dynamometer, and it was arranged on the worktable of the grinder. Given the significant impact force exerted by the diamond abrasive grains during grinding, the original signal required low-frequency filtering [24]. The average value of the smoothed signal during the steady-state phase was calculated as the grinding force.

The grinding of the samples was carried out under dry grinding conditions, with the grinding parameters listed in Table 2. After completing each set of the grinding test, the grinding wheel cooled down, and the wear condition was observed. If severe wear occurred, the wheel was subjected to dressing.

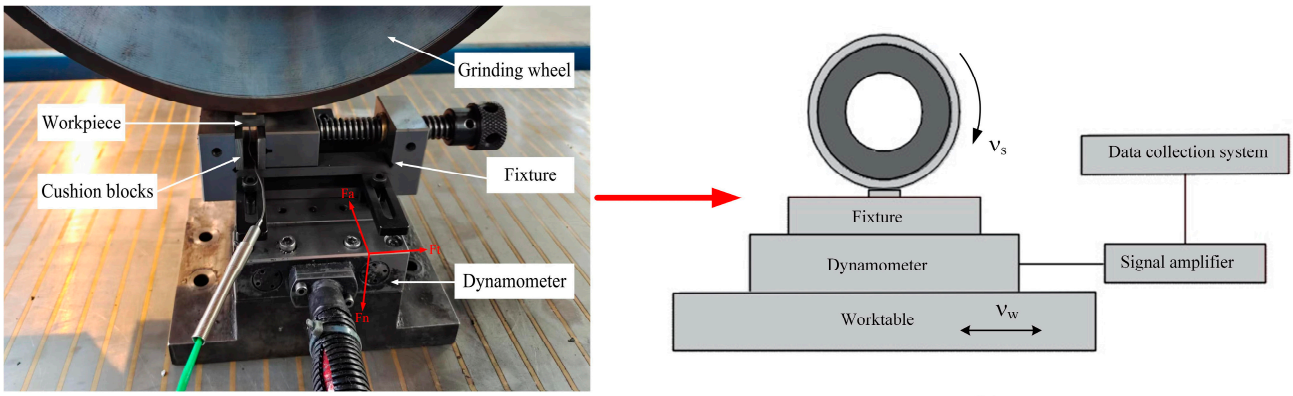


Figure 3. Grinding system: (**a**) the composition of the grinding system, (**b**) simplified diagram of the grinding system.

Table 2. Grinding parameters.

Grinding Wheel Speed *vs.* (m/s)	Workpiece Feed Speed *vw* (m/min)	Grinding Depth a_p (μm)
30.14	6	10, 30, 50, 70, 90, 110

2.3. Ground Surface Integrity Test

The characteristics of surface integrity were examined and compared at different grinding depths. A white light interferometer (Contour Elite K, Madison, WI, USA) was used to determine the surface roughness parameters Ra and Rz. Meanwhile, the morphology of the ground surfaces and subsurface was observed using scanning electron microscopy (SEM) and ultra-depth field electron microscopy (VHX-5000). The elemental content and composition were also obtained by EDS energy spectrometry.

The surface residual stresses under different grinding depths were determined using a D8 ADVANCE X-ray diffractometer (XRD) (Bruker, Billerica, MA, USA) with Co-Kα radiation. Due to the relatively low content of the HEA binder phase, the stress testing was performed on the (101) diffraction plane of WC, corresponding to a diffraction angle of 2θ = 56.78°. Stress testing was conducted using the $\sin^2\psi$ method [25], with the tilt angle ψ set in the range of 0 to 45° in 6 groups, corresponding to 0°, 9°, 18°, 27°, 36°, and 45°, as shown in Table 3.

Table 3. Residual stress testing parameters.

Grinding Depth (μm)	Angle ψ (°)
10	0, 9, 18, 27, 36, 45
30	0, 9, 18, 27, 36, 45
50	0, 9, 18, 27, 36, 45
70	0, 9, 18, 27, 36, 45
90	0, 9, 18, 27, 36, 45
110	0, 9, 18, 27, 36, 45

To assess the impact of grinding on the flexural strength and surface hardness, three-point bending tests and microhardness tests were conducted, respectively. Before the three-point bending test, the original ground samples were cut into thin slices with a thickness of 2 mm, which were taken as the bending test sample. Figure 4 illustrates the schematic diagram of the test. The slices were chamfered and then placed on the universal testing machine (AGS-X5KN) with a support span of 15 mm. The load was applied to the center of the slice specimen at a rate of 5 mm/min until fracture occurred. The maximum

load value was recorded during the test, and the bending strength [26] of the slice specimen was calculated using Equation (2):

$$\sigma_b = \frac{3PL}{2bh^2} \quad (2)$$

where σ_b is the bending strength (MPa); P is the critical load at which the slice specimen fractures; L is the support span; b is the width of the slice specimen; and h is the thickness of the sliced specimen.

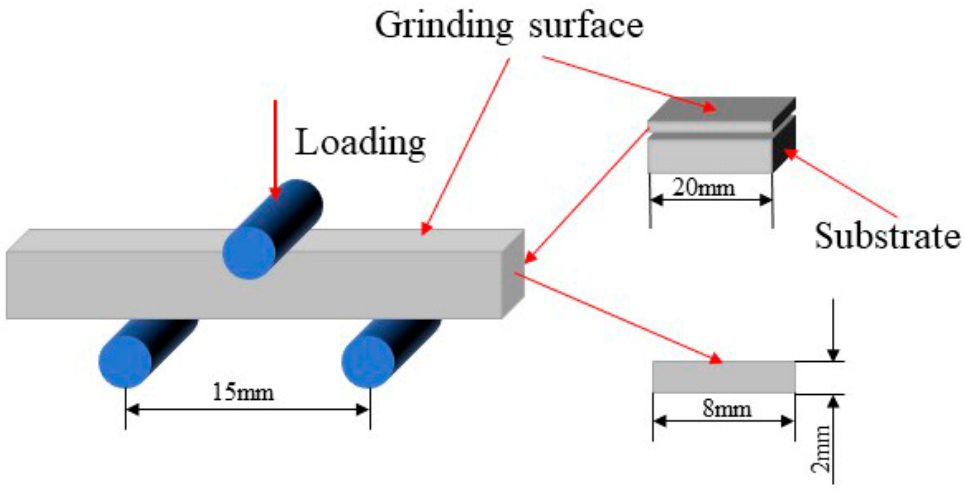


Figure 4. Three-point bending test.

Microhardness values at the cross-section under different processing parameters were obtained employing a Vickers hardness tester (HXD-1000TMC (Taiming, Shanghai, China)). Measurements were taken every 15 μm, with a load of 1.96 N applied for 15 s to ensure constant pressure. The degree of work hardening of the ground surface is calculated using Equation (3):

$$N = \frac{HV}{HV_0} \times 100\% \quad (3)$$

where N is the degree of hardening of the machined surface; HV is the microhardness of the machined surface; and HV_0 is the microhardness of the unmachined surface of the WC-HEA alloy.

3. Results and Discussion

3.1. Grinding Force

The grinding experiments recorded three components of the grinding forces, including the axial grinding force (*Fa*), the tangential grinding force (*Ft*), and the normal grinding force (*Fn*). The directions of the grinding forces are illustrated in Figure 3. Since the axial grinding force does not vary significantly with the increase in grinding depth, it is not considered in the analysis of grinding forces. The grinding force quantitatively reflects the extent of interaction between the grinding wheel and the workpiece during the material removal process of WC-HEA alloys [27,28]. Factors such as grinding wheel wear, material removal rate, and surface integrity (surface morphology, surface roughness, residual stress, etc.) are significantly influenced by the grinding force. As the real-time monitoring data in the grinding process, the tangential force and normal force under different grinding depths increase with the increase in a_p, with the normal force being much greater than the tangential force, as shown in Figure 5.

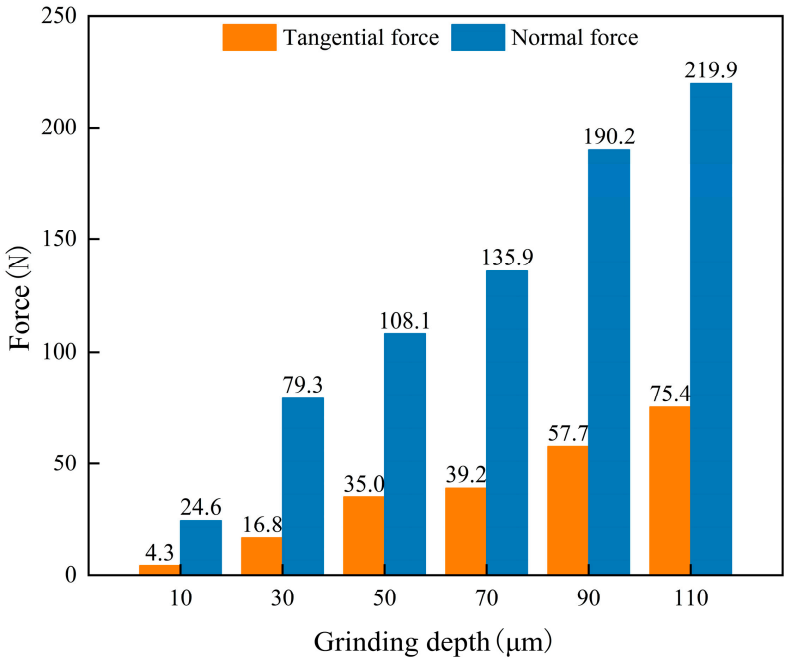


Figure 5. Normal force and tangential force at various grinding depths.

3.2. Surface Morphology and Material Removal Mechanism

Figure 6 illustrates the variations in surface morphology resulting from grinding at different depths. In Figure 6a, narrow and deep scratches are visible, accompanied by bulges on either side and a noticeably smooth region at the bottom of the scratches. Figure 6b displays a stack of flaked layers, while in Figure 6c, extensive breakouts are observed, although not completely detached from the surface. As the grinding depth increases further, Figure 6d depicts a relatively flat ground surface, with the scratches transitioning from deep to shallow and becoming less dense.

The surface morphology of WC-HEA exhibits significant differences compared to the traditional WC-Co. In single grain cutting test of the traditional WC-Co, the extension of cracks in WC leads to material fracture, delamination, and eventually fracture, followed by a transition to a plastic removal mechanism [15]. When the a_p = 10 μm, under this grinding depth, plastic deformation characterized by plowing predominates, with slip lines present at the bottom of the groove indicating extensive plastic flow. However, due to the dynamic impact of the diamond grinding wheel, partial fragmentation occurs at the raised positions. When the a_p > 10 μm, microcracks are generated on the ground surface, and the expansion of these microcracks leads to brittle removal characterized by delamination and fragmentation. Microcracks only result in the brittle removal of the material without extending into macroscopic cracks, thereby preventing damage to the ground surface. When the a_p = 110 μm, WC experiences a transgranular or intergranular fracture, leading to the formation of finer grains and thus avoiding the occurrence of macroscopic cracks and large fractures. In Figure 7, the arrows indicate WC grain damage caused by grinding, primarily consisting of microcracks and fractures.

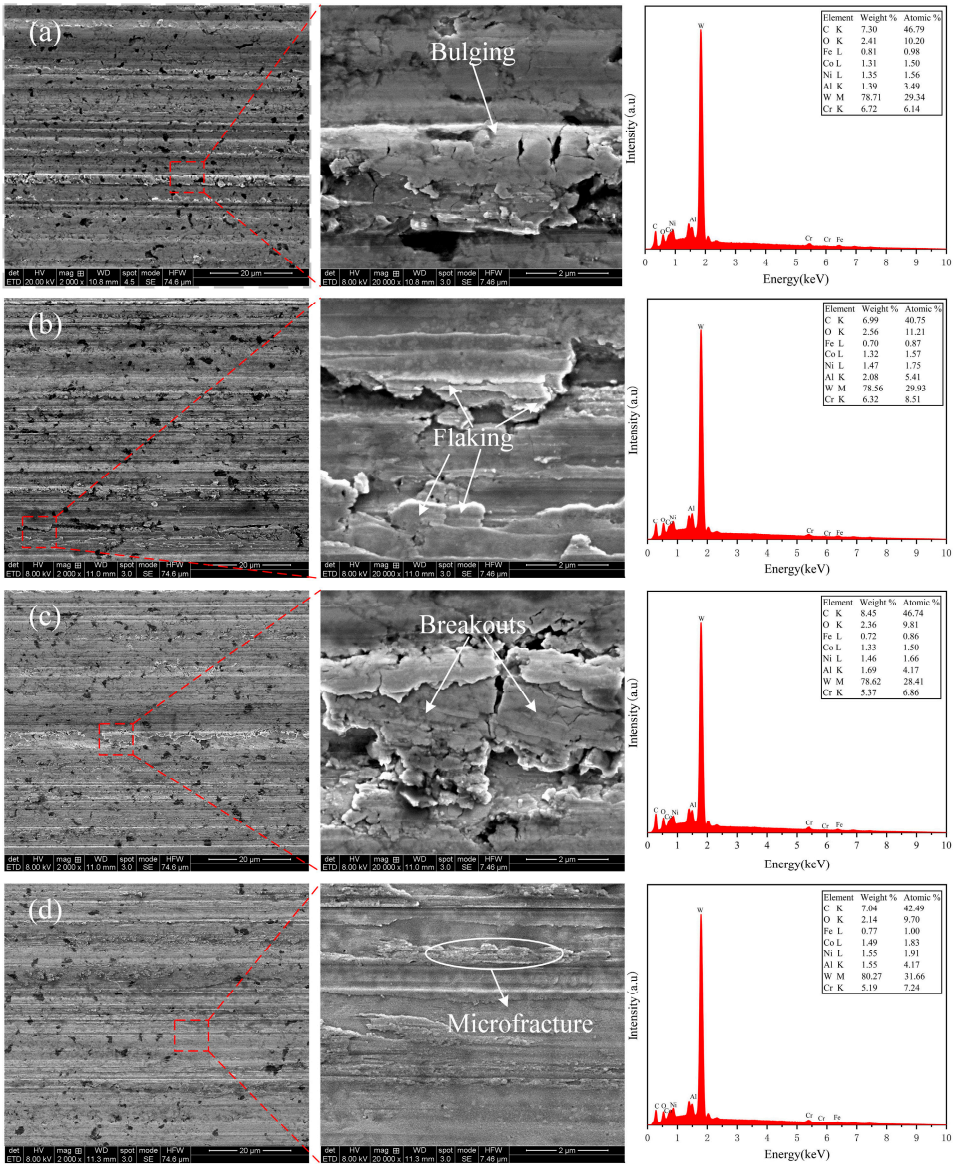


Figure 6. Surface morphology and EDS content of WC-HEA cemented carbide after grinding: (**a**) a_p = 10 μm, (**b**) a_p = 30 μm, (**c**) a_p = 50 μm, and (**d**) a_p = 110 μm.

The EDS analysis of the ground surface further confirmed the material removal mechanism. Figure 8 depicts the fracture surface of the WC-HEA cemented carbide, where Figure 8a shows the morphology of the fracture, and Figure 8b displays the elemental composition and content at the fracture site. Table 4 provides a quantitative comparison between the elemental composition at the fracture site and the ground surface, revealing a decrease in the content of the HEA binder phase composed of Al, Co, Cr, Fe, and Ni elements. This is in contrast to the ground surface of the WC-Co alloy, where the presence of Co, with its good ductility, results in a coating of fractured WC on the surface, especially at the protrusions, leading to high Co contents [10,11]. Under the impact of diamond abrasive grains, both the WC grains serving as the framework and the HEA binder phase in the WC-HEA alloy undergo removal.

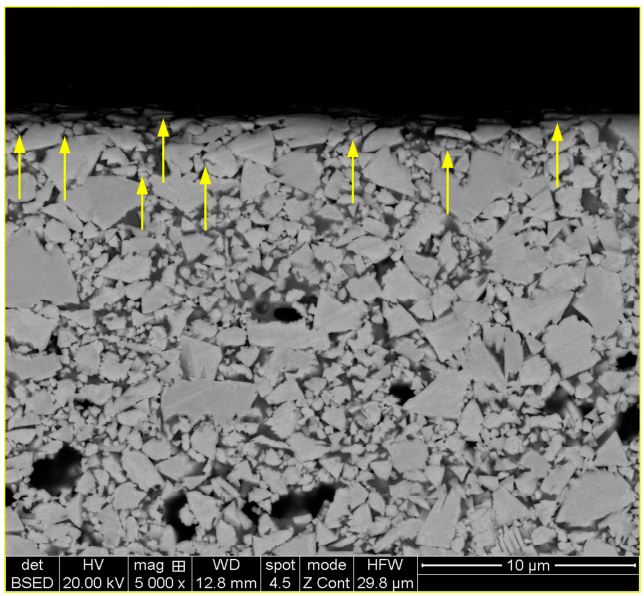


Figure 7. The crack features and distribution on the ground surface with a_p = 110 µm.

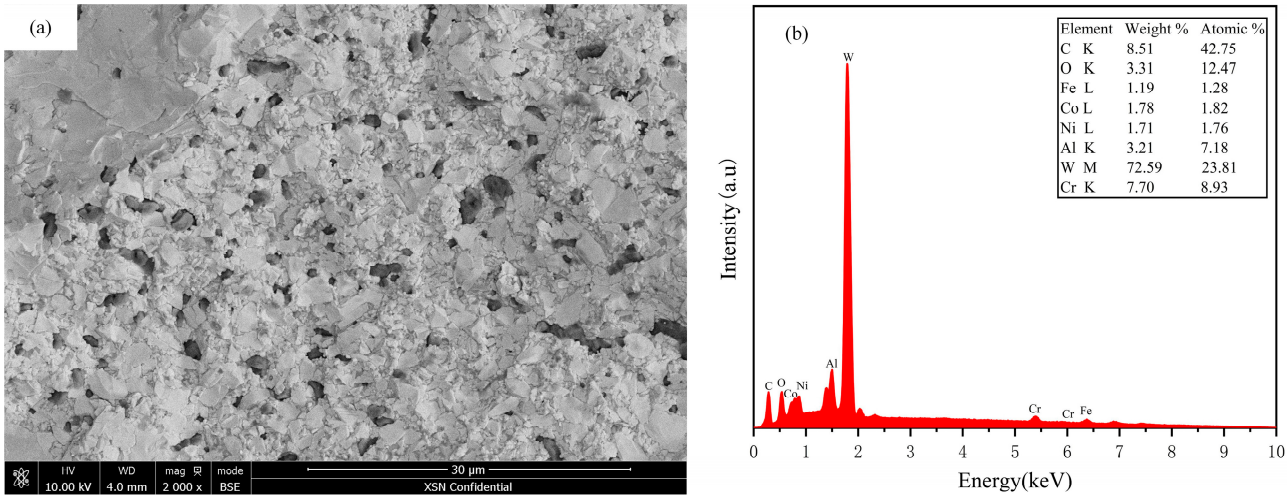


Figure 8. Fracture analysis of WC-HEA cemented carbide: (**a**) Fracture morphology; (**b**) elemental composition and content of the fracture.

Table 4. The elemental composition and content.

Element	Fracture (wt.%)	a_p = 10 µm (wt.%)	a_p = 30 µm (wt.%)	a_p = 50 µm (wt.%)	a_p = 110 µm (wt.%)
C $_K$	8.51	7.30	6.99	8.45	7.04
O $_K$	3.31	2.41	2.56	2.36	2.14
Fe $_L$	1.19	0.81	0.70	0.72	0.77
Co $_L$	1.78	1.31	1.32	1.33	1.49
Ni $_L$	1.71	1.35	1.47	1.46	1.55
Al $_K$	3.21	1.39	2.08	1.69	1.55
W $_M$	72.59	78.71	78.56	78.62	80.27
Cr $_K$	7.7	6.72	6.32	5.37	5.19

Grinding alters surface morphology. However, whether there are changes in the morphology below the ground surface requires further investigation. The cross-section obtained by wire cutting was observed after polishing using a digital microscope with an extended depth of field (VHX-5000), revealing the deformed layer below the ground surface, as depicted in Figure 9a. Following polishing, the section was subjected to corrosion treatment using a mixed solution containing 20% K3[Fe (CN)6] and 20% KOH, resulting in the metallographic structure shown in Figure 9b. A comparison between the subsurface below the ground surface and the substrate revealed grain refinement in the subsurface of the WC-HEA. This grain refinement was attributed to severe plastic deformation induced by the coupling effect of diamond grain compression and grinding heat.

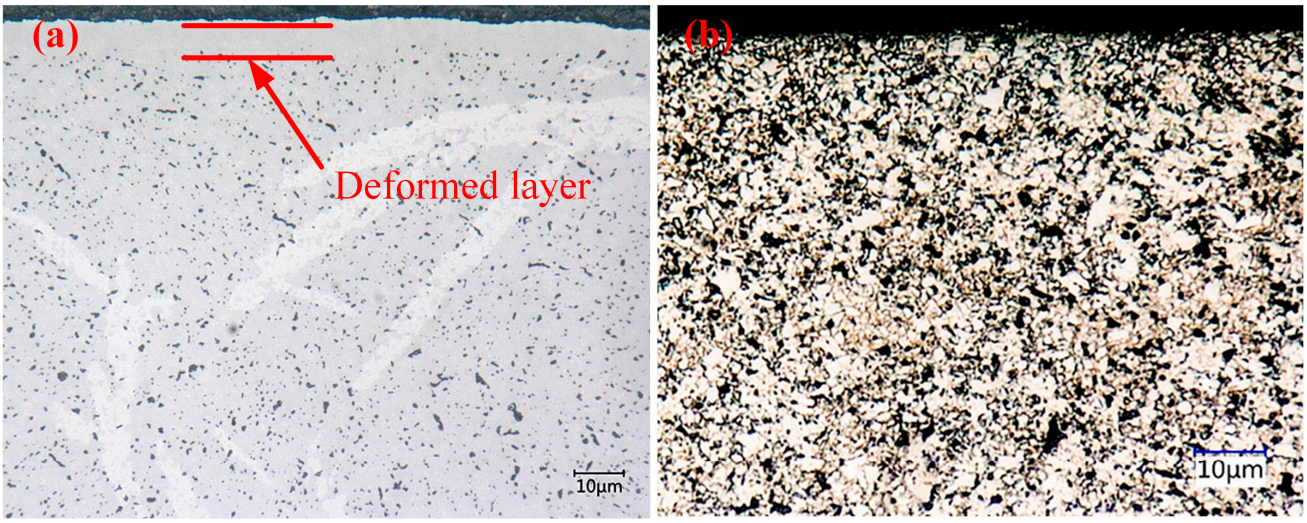


Figure 9. Subsurface morphology: (**a**) Deformed layer; (**b**) metallographic structure after corrosion.

3.3. Surface Roughness

Surface roughness serves as a visual reflection of surface morphology, with the three-dimensional morphology of the ground surface depicted in Figure 10. Due to the material removal achieved by the cutting action of abrasive grains, microscopic scratches are distributed across the ground surface. As observed in Figure 10, there exists a height difference between the bottom of the WC-HEA hard alloy grooves and the protrusions caused by plowing, with a smaller grinding depth corresponding to a larger height difference and, consequently, a higher surface roughness. With the increase in cutting depth, the distance between the grooves increases, leading to a smoother fluctuation in the height of surface peaks and valleys, while the surface pits and grinding damage gradually decrease, resulting in a reduction in surface roughness.

The surface roughness measurement results are depicted in Figure 11. With an increase in grinding depth from 10 μm to 110 μm, the surface roughness Ra decreases from 0.66 μm to 0.48 μm, and the surface roughness Rz decreases from 6.52 μm to 4.58 μm. And as the a_p increases, there is a corresponding increase in the contact length between the wheel and the workpiece, allowing a greater number of abrasive grains to participate in the cutting process. This results in an increase in material removal rate and a subsequent reduction in surface roughness. Furthermore, the heightened grinding depth amplifies the compressive force exerted by the grinding wheel on the workpiece material surface, leading to an escalation in the grinding force.

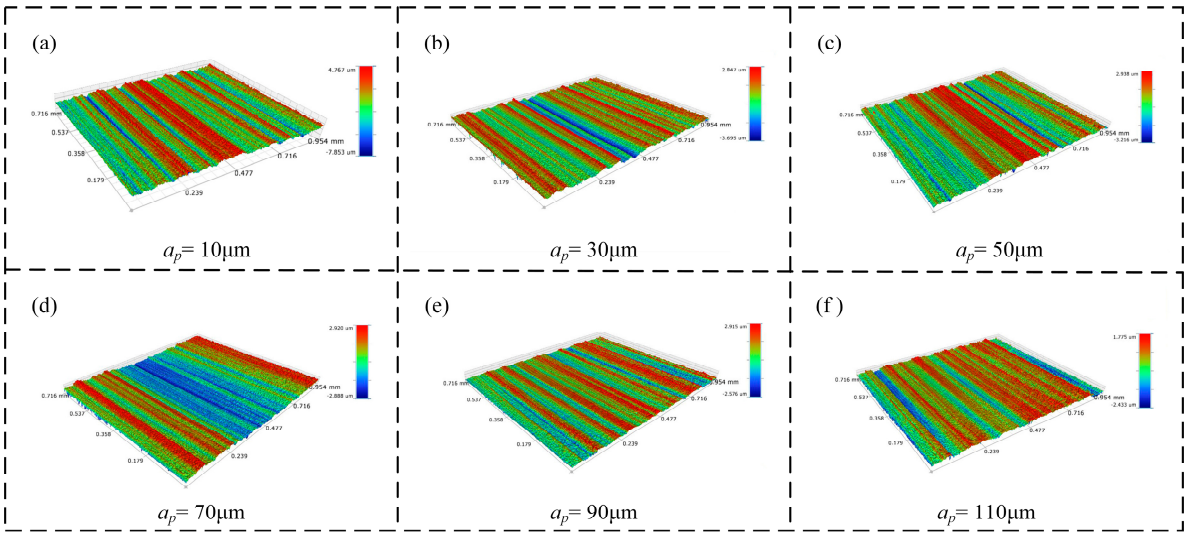


Figure 10. The three-dimensional morphology of the machined surface at different grinding depths, (**a**–**f**) respectively represent a_p from 10 to 110 μm.

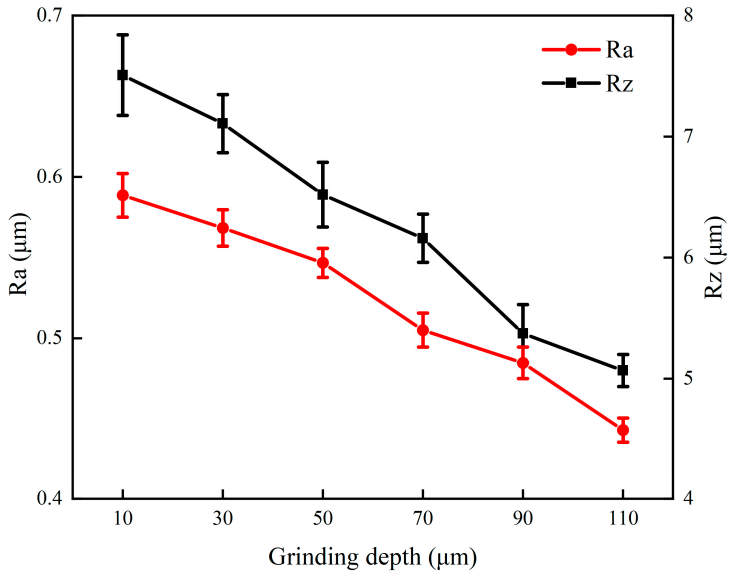


Figure 11. Surface roughness parameters Ra and Rz at different depths of grinding.

3.4. Surface Residual Stress

Figure 12 shows X-ray diffraction spectra of the ground surface with a_p = 10 μm at different angles. Compared to the XRD pattern at 0°, a shift in the diffraction peaks is observed with varying ψ-angles. According to Bragg's law, the peak shift is related to residual stress. The rightward shift in the diffraction peaks, associated with an increase in the diffraction angle, results in a decrease in the interplanar spacing d and an increase in the micro-strain of WC grains [29].

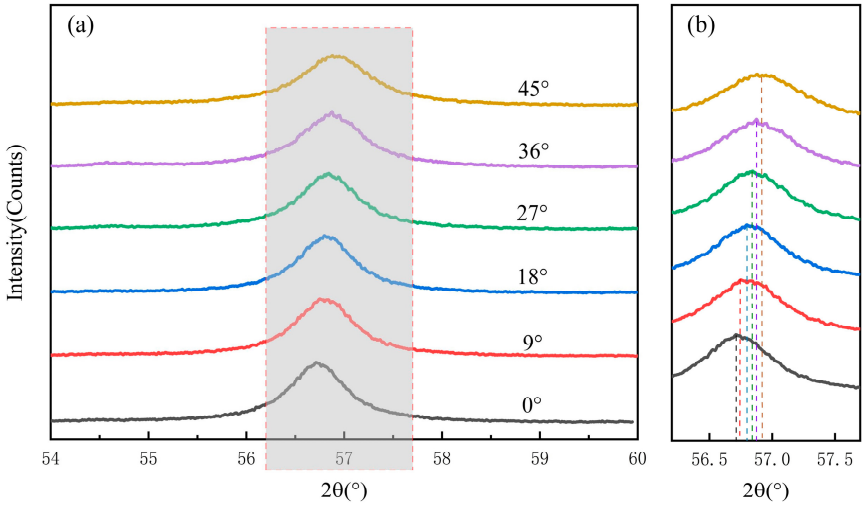


Figure 12. XRD patterns at a_p = 10μm; (**a**) presents the XRD patterns at different angles in the same direction, and (**b**) presents a magnified view of the local region.

The samples prepared by powder metallurgy processes exhibit residual stresses after sintering [29], which are altered during the grinding process, changing their original stress state. Due to the relatively small sintering residual stresses and under large grinding depths, the sintering residual stresses can be effectively eliminated. Similarly to the findings of Hegeman [11] and Yang [19], Figure 13 illustrates that the residual stresses generated during the grinding process are compressive in nature. With increasing a_p, the residual compressive stresses intensify, reaching a maximum residual compressive stress of 1795 MPa.

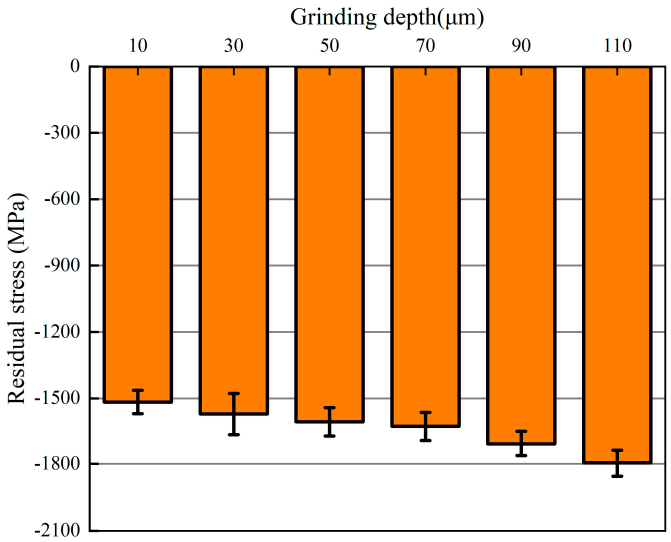


Figure 13. Influence of different grinding depths on residual stress of ground surface.

Plastic deformation on the machined surface and grinding heat are the primary causes of residual stresses. Generally, thermal loads are more likely to lead to residual tensile stresses, while plastic deformation and mechanical loads are the main contributors to residual tensile stresses [30,31]. Residual grinding stresses result from uneven plastic deformation under the coupling of grinding force and grinding heat, and these stresses are released through cracks and plastic deformation within WC grains. The compressive field is formed radially due to the squeezing action of the diamond abrasive particles at the tip of the grinding wheel. Microcracks are initially generated, and as the a_p increases, these microcracks extend to form macroscopic cracks, resulting in the production of large fragments and brittle fractures. With the increase in grinding depth, tangential tension is

generated in the plastic deformation zone around the contact point of the diamond tip, and plastic shear becomes significant, especially at large grinding depths. In the grinding process, both mechanical and thermal loads are present. The plastic deformation caused by the combined effects of the grinding wheel's squeezing action and the cutting action of diamond abrasive particles weakens the tensile stresses induced by thermal loads.

3.5. Three-Point Bending Test

In practical applications, cemented carbides are subjected to bending loads [32]. Therefore, the bending strength of the machined surface was determined through three-point bending tests [19,33]. This strength was calculated using Equation (2), and Figure 14 illustrates the bending strength of the ground surface at different grinding depths. Clearly, the bending strength of the ground surface has been improved to varying degrees when compared to the original material strength of 890 MPa. Moreover, under the machining parameter of a grinding depth of 110 μm, the bending strength is the highest, reaching 1039 MPa and representing an increase of approximately 16.7% compared to the unmachined surface.

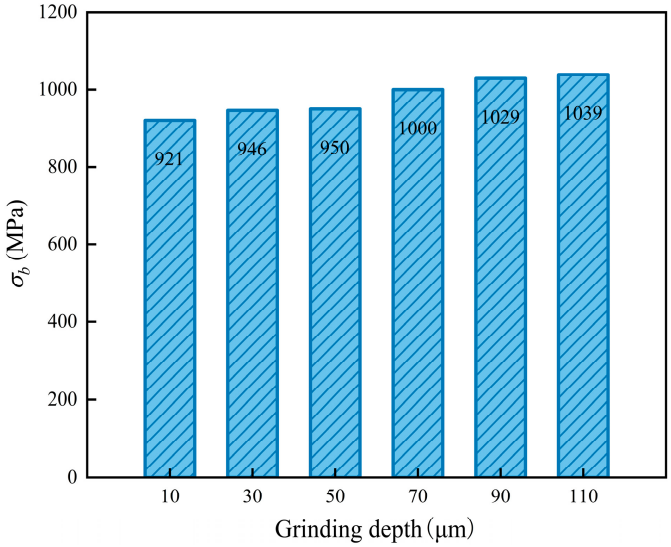


Figure 14. Bending strength of the ground surface at different grinding depths.

Comparing the variation trends of residual stress values on the ground surface, an interesting finding emerged: The increase in residual compressive stress on the ground surface appears to affect the bending strength of the ground surface. Similar conclusions have been drawn from the grinding process of WC-Co cemented carbide [20]. According to SEM observations of the fracture surface, the main cause of fracture is attributed to internal defects in the material, such as the clustering of WC grains and porosity [34]. Residual compressive stress plays a role in suppressing the occurrence of fractures caused by internal defects in the material, leading to an increase in the strength of the ground surface.

3.6. Microhardness

Figure 15a indicates that the microhardness of the ground surface increases with the increase in a_p, and the depth of the processed hardened layer is approximately 180 μm. The microhardness of the ground surface is higher than that of the substrate, and the microhardness shows an overall decreasing trend along the grinding depth direction, gradually approaching the hardness of the matrix. However, the microhardness sharply decreases at a distance of 15 μm from the ground surface, which is primarily attributed to grinding heat [35]. As the grinding process employs dry grinding without the use of cooling fluid, a small portion of heat is carried away with the grinding debris, while a significant amount of heat remains trapped on the ground surface. This heat causes thermal

softening in the thin layer of the WC-HEA alloy, offsetting some of the hardening effects. As the influence of grinding heat weakens along the grinding depth, the microhardness gradually decreases to approach the hardness of the matrix at a distance of 30 μm from the ground surface.

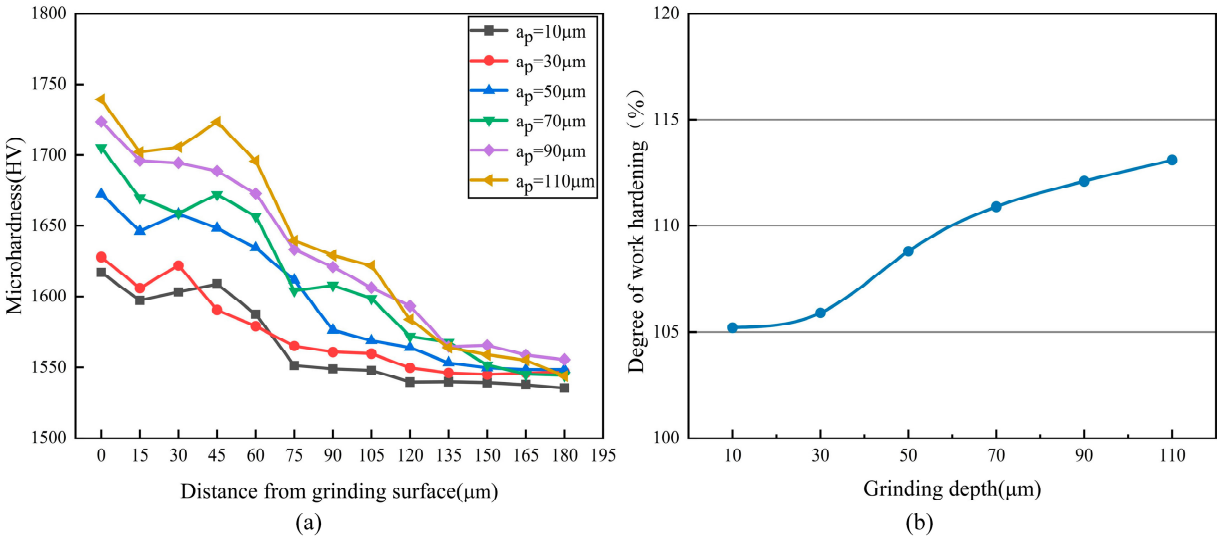


Figure 15. Impact of grinding depth on surface hardness: (**a**) Microhardness distribution along the cutting depth direction; (**b**) degree of work hardening.

The degree of surface hardening of the ground surface was calculated using Equation (3), and Figure 15b illustrates a hardening degree ranging from 105.2% to 113.1%. With increasing a_p, the microhardness of the ground surface increased, indicating a more pronounced degree of work hardening. The proportion of thermal softening layer caused by grinding heat within the work-hardened layer was minimal, thus having an insignificant impact on the work-hardened layer. Microhardness values were restored at a depth of 30 μm below the ground surface. During the grinding process, the ground surface experienced the compression and impact of abrasive grains, primarily due to mechanical loading, resulting in plastic deformation. With the continuous increase in plastic deformation, lattice distortion occurred, leading to grain refinement.

4. Conclusions

In the current research, the material removal mechanisms and surface integrity during the grinding process of fine-grained WC-15wt%$Al_{0.5}$CoCrFeNi cemented carbide were investigated and discussed. The following conclusions were obtained:

(1) During the grinding process, both the HEA binder phase and the WC are simultaneously removed, undergoing a transition from ductile removal to brittle removal, with brittle removal being predominant.
(2) A subsurface deformed layer is found, characterized primarily by refined WC grains.
(3) Surface roughness serves as a direct reflection of surface morphology. It decreases with an increase in grinding depth. A larger depth of grind is an effective machining parameter for achieving high surface quality, as it increases the contact arc length, resulting in a higher number of abrasive grains participating in the cutting process and consequently increasing the material removal rate.
(4) Grinding introduces high compressive stresses onto the surface, with a maximum compressive stress of 1795 MPa. The enhancement of bending strength relies on residual compressive stresses.
(5) Grinding induces surface work hardening, with a hardening layer depth of approximately 180 μm. The degree of work hardening on the ground surface increases with larger depths of cut, reaching a maximum of 113.1%.

Author Contributions: Conceptualization, Y.Y. and J.D.; methodology, Y.Y., J.D. and P.Z.; software, Y.Y. and Y.X.; validation, Y.S.; investigation, Y.Y. and J.D.; writing—original draft, Y.Y.; writing—review and editing, J.D. and G.S.; supervision, J.D., Y.S., Y.X., P.Z. and G.S. All authors have read and agreed to the published version of the manuscript.

Funding: This work was supported by the Natural Science Foundation of China (52275438,51675289), the Natural Science Foundation of Shandong Province (ZR2020ME160) and the Basic research project of the pilot project of the integration of science, education and production (Qilu University of Technology (Shandong Academy of Sciences)) (2022PY007, 2022PX044, 2023PY021, 2023PX026).

Data Availability Statement: The raw data supporting the conclusions of this article will be made available by the authors on request.

Conflicts of Interest: The authors declare no conflict of interest.

References

1. Yang, Y.; Zhang, C.; Wang, D.; Nie, L.; Wellmann, D.; Tian, Y. Additive manufacturing of WC-Co hardmetals: A review. *Int. J. Adv. Manuf. Technol.* **2020**, *108*, 1653–1673. [CrossRef]
2. Sun, I.; Zhao, J.; Huang, Z.; Yan, K.; Shen, X.; Xing, J.; Gao, Y.; Jian, Y.; Yang, H.; Li, B. A Review on Binderless Tungsten Carbide: Development and Application. *Nano-Micro Lett.* **2020**, *12*, 1–37. [CrossRef] [PubMed]
3. García, J.; Collado Ciprés, V.; Blomqvist, A.; Kaplan, B. Cemented carbide microstructures: A review. *Int. J. Refract. Met. Hard Mater.* **2019**, *80*, 40–68. [CrossRef]
4. Yu, P.F.; Zhang, L.J.; Cheng, H.; Zhang, H.; Ma, M.Z.; Li, Y.C.; Li, G.; Liaw, P.K.; Liu, R.P. The high-entropy alloys with high hardness and soft magnetic property prepared by mechanical alloying and high-pressure sintering. *Intermetallics* **2016**, *70*, 82–87. [CrossRef]
5. Juan, C.; Hsu, C.; Tsai, C.; Wang, W.; Sheu, T.; Yeh, J.; Chen, S. On microstructure and mechanical performance of AlCoCr-FeMo0.5Nix high-entropy alloys. *Intermetallics* **2013**, *32*, 401–407. [CrossRef]
6. Kim, Y.; Joo, Y.; Kim, H.S.; Lee, K. High temperature oxidation behavior of Cr-Mn-Fe-Co-Ni high entropy alloy. *Intermetallics* **2018**, *98*, 45–53. [CrossRef]
7. Chuang, M.; Tsai, M.; Wang, W.; Lin, S.; Yeh, J. Microstructure and wear behavior of AlxCo1.5CrFeNi1.5Tiy high-entropy alloys. *Acta Mater.* **2011**, *59*, 6308–6317. [CrossRef]
8. Chen, C.; Yang, C.; Chai, H.; Yeh, J.; Chau, J.L.H. Novel cermet material of WC/multi-element alloy. *Int. J. Refract. Met. Hard Mater.* **2014**, *43*, 200–204. [CrossRef]
9. Zhou, P.; Xiao, D.; Yuan, T. Comparison between ultrafine-grained WC—Co and WC—HEA-cemented carbides. *Powder Metall.* **2017**, *60*, 1–6. [CrossRef]
10. Byrne, G.; Dornfeld, D.; Denkena, B.; Denkena, B. Advancing Cutting Technology. *CIRP Ann.* **2003**, *52*, 483–507. [CrossRef]
11. Hegeman, J.B.J.W.; De Hosson, J.T.M.; De With, G. Grinding of WC–Co hardmetals. *Wear* **2001**, *248*, 187–196. [CrossRef]
12. Zhu, Y.; Zhang, Q.; Zhao, Q.; To, S. The material removal and the nanometric surface characteristics formation mechanism of TiC/Ni cermet in ultra-precision grinding. *Int. J. Refract. Met. Hard Mater.* **2021**, *96*, 105494. [CrossRef]
13. Wei, C.; He, C.; Chen, G.; Sun, Y.; Ren, C. Material removal mechanism and corresponding models in the grinding process: A critical review. *J. Manuf. Process.* **2023**, *103*, 354–392. [CrossRef]
14. Klocke, F.; Wirtz, C.; Mueller, S.; Mattfeld, P. Analysis of the Material Behavior of Cemented Carbides (WC-Co) in Grinding by Single Grain Cutting Tests. *Procedia Cirp.* **2016**, *46*, 209–213. [CrossRef]
15. Wirtz, C.; Mueller, S.; Mattfeld, P.; Klocke, F. A Discussion on Material Removal Mechanisms in Grinding of Cemented Carbides. *J. Manuf. Sci. Eng.* **2017**, *139*, 121002. [CrossRef]
16. Mueller, S.; Wirtz, C.; Trauth, D.; Mattfeld, P.; Klocke, F. Material removal mechanisms in grinding of two-phase brittle materials. *Int. J. Adv. Manuf. Technol.* **2018**, *95*, 287–298. [CrossRef]
17. Huang, H.; Li, X.; Mu, D.; Lawn, B.R. Science and art of ductile grinding of brittle solids. *Int. J. Mach. Tools Manuf.* **2021**, *161*, 103675. [CrossRef]
18. Yang, J.; Roa, J.J.; Schwind, M.; Odén, M.; Johansson-Jõesaar, M.P.; Llanes, L. Grinding-induced metallurgical alterations in the binder phase of WC-Co cemented carbides. *Mater. Charact.* **2017**, *134*, 302–310. [CrossRef]
19. Yang, J.; Odén, M.; Johansson-Jõesaar, M.P.; Llanes, L. Grinding Effects on Surface Integrity and Mechanical Strength of WC-Co Cemented Carbides. *Procedia Cirp.* **2014**, *13*, 257–263. [CrossRef]
20. Yin, L.; Spowage, A.C.; Ramesh, K.; Huang, H.; Pickering, J.P.; Vancoille, E.Y.J. Influence of microstructure on ultraprecision grinding of cemented carbides. *Int. J. Mach. Tools Manuf.* **2004**, *44*, 533–543. [CrossRef]
21. Zhang, Q.; To, S.; Zhao, Q.; Guo, B.; Wu, M. Effects of binder addition on the surface generation mechanism of WC/Co during high spindle speed grinding (HSSG). *Int. J. Refract. Met. Hard Mater.* **2016**, *59*, 32–39. [CrossRef]
22. Liang, F.; Du, J.; Su, G.; Zhang, P.; Zhang, C. Investigating the effect of Al, Mo or Mn addition to CoCrFeNi entropy alloys on the interface binding properties of WC/HEA cemented carbides. *Mater. Today Commun.* **2023**, *35*, 105891. [CrossRef]

23. Luo, W.; Liu, Y.; Shen, J. Effects of binders on the microstructures and mechanical properties of ultrafine WC-10%AlxCoCrCuFeNi composites by spark plasma sintering. *J. Alloys Compd.* **2019**, *791*, 540–549. [CrossRef]
24. Ghosh, N.; Ravi, Y.B.; Patra, A.; Mukhopadhyay, S.; Paul, S.; Mohanty, A.R.; Chattopadhyay, A.B. Estimation of tool wear during CNC milling using neural network-based sensor fusion. *Mech. Syst. Signal Pr.* **2007**, *21*, 466–479. [CrossRef]
25. Luo, Q.; Jones, A.H. High-precision determination of residual stress of polycrystalline coatings using optimised XRD-sin2ψ technique. *Surf. Coat. Technol.* **2010**, *205*, 1403–1408. [CrossRef]
26. Li, A.; Zhao, J.; Wang, D.; Gao, X.; Tang, H. Three-point bending fatigue behavior of WC–Co cemented carbides. *Mater. Design.* **2013**, *45*, 271–278. [CrossRef]
27. Zhou, K.; Ding, H.H.; Wang, W.J.; Wang, R.X.; Guo, J.; Liu, Q.Y. Influence of grinding pressure on removal behaviours of rail material. *Tribol. Int.* **2019**, *134*, 417–426. [CrossRef]
28. Zhang, Y.; Li, C.; Ji, H.; Yang, X.; Yang, M.; Jia, D.; Zhang, X.; Li, R.; Wang, J. Analysis of grinding mechanics and improved predictive force model based on material-removal and plastic-stacking mechanisms. *Int. J. Mach. Tools Manuf.* **2017**, *122*, 81–97. [CrossRef]
29. Guezmil, M.; Bensalah, W.; Mezlini, S. Tribological behavior of UHMWPE against TiAl6V4 and CoCr28Mo alloys under dry and lubricated conditions. *J. Mech. Behav. Biomed.* **2016**, *63*, 375–385. [CrossRef]
30. Krawitz, A.; Drake, E. Residual stresses in cemented carbides—An overview. *Int. J. Refract. Met. Hard Mater.* **2015**, *49*, 27–35. [CrossRef]
31. Elsheikh, A.H.; Shanmugan, S.; Muthuramalingam, T.; Thakur, A.K.; Essa, F.A.; Ibrahim, A.M.M.; Mosleh, A.O. A comprehensive review on residual stresses in turning. *Adv. Manuf.* **2022**, *10*, 287–312. [CrossRef]
32. Torres, Y.; Sarin, V.K.; Anglada, M.; Llanes, L. Loading mode effects on the fracture toughness and fatigue crack growth resistance of WC–Co cemented carbides. *Scripta Mater.* **2005**, *52*, 1087–1091. [CrossRef]
33. Wang, J.; Bai, X.; Shen, X.; Liu, X.; Wang, B. Effect of micro-texture on substrate surface on adhesion performance of electroless Ni P coating. *J. Manuf. Process.* **2022**, *74*, 296–307. [CrossRef]
34. Torres, Y.; Anglada, M.; Llanes, L. Fatigue mechanics of WC–Co cemented carbides. *Int. J. Refract. Met. Hard Mater.* **2001**, *19*, 341–348. [CrossRef]
35. Heinzel, C.; Bleil, N. The Use of the Size Effect in Grinding for Work-hardening. *CIRP Ann.* **2007**, *56*, 327–330. [CrossRef]

Disclaimer/Publisher's Note: The statements, opinions and data contained in all publications are solely those of the individual author(s) and contributor(s) and not of MDPI and/or the editor(s). MDPI and/or the editor(s) disclaim responsibility for any injury to people or property resulting from any ideas, methods, instructions or products referred to in the content.